scientific reports

OPEN

Wideband filtering antenna loading U-shaped parasitic patches based on characteristic mode analysis

Wen Huang[1✉], Pengfei Wang[1,2], Jie Hu[1,2] & Shengwei Hou[1,2]

A wideband filtering antenna loading with U-shaped parasitic patches (UPP) is proposed by the characteristic mode analysis (CMA). The antenna is consisted of two dielectric substrates, one of which is printed with an eight-sawteeth patch, four single-sawteeth patches and two pairs of U-shaped parasitic patches. The sawteeth structures enable the two distinct characteristic modes to be closer with a smaller frequency space while allowing them to coexist within the operating frequency band, significantly enhancing the bandwidth. The two pairs of UPP can generate low-frequency and high-frequency radiation nulls, respectively. Utilizing CMA, potential modal nulls are identified at 4 GHz in the low stopband and at 7.5 GHz in the high stopband. Upon excitation with an L-shaped probe, the antenna exhibits radiation nulls precisely at 4 GHz and 7.41 GHz. The antenna's dimensions are $0.94\lambda_0 \times 0.94\lambda_0 \times 0.066\lambda_0$ (50 mm×50 mm×2.5 mm), where λ_0 represents the wavelength of the center frequency in free space. The measured impedance bandwidth with $|S_{11}|$ below − 10 dB is 26.38% (5 GHz to 6.52 GHz). The gain in the operational bandwidth is fluctuated from 7.21 dBi to 7.98 dBi, while the out-of-band suppression is reached 12.3 dB at a low frequency band and 17.8 dB at a high frequency band. Within the bandwidth range, the cross-polarization level remains under − 31 dB. The proposed antenna characterized by broadband, low cross-polarization, and low-profile, can be widely applied in 5G communication.

A filtering antenna is a kind antenna that combines both radiation and filtering functions. In traditional communication systems, the filter and antenna are typically separated, leading to a larger size and a higher insertion loss [1]. Consequently, the utilization of filtering antennas has become more widespread. The design of integrated filtering antennas is currently a hot research topic in the communication field, owing to their capability to minimize size, enhance system integration, and mitigate insertion loss. Nevertheless, achieving antennas with filtering capacity is encountered a numerous challenge, especially when considering the requirements of a wide impedance bandwidth and a low profile.

To realize an antenna with filtering capability, there are three primary schemes. Scheme 1 involves the incorporation of filtering structures in the antenna's feeding network. According to the reference[2], by introducing two pairs of notch elements into the feeding structure, three radiation nulls are generated, thereby making the feeding structure with filtering function. However, this feeding structure is complex. In reference[3], a microstrip feeding line with an open-circuit stub is adopted to generate a radiation null in the upper stopband. However, the integration of the filtering structure into the feeding structure inevitably leads to increased insertion loss. In the Scheme 2, an antenna is used to instead of the final resonator of the filter. As discussed in the reference[4], Chuang proposed a co-design methodology for filtering antenna by integrating a filter with an antenna. Nevertheless, the implementation of this method frequently necessitates the inclusion of several resonators to achieve the filtering function, subsequently leading to in additional loss and a larger circuit size. In reference[5], additional coupling is induced between the source/load and non-adjacent resonators to construct cross-coupling paths. Through these cross-coupling paths, the filtering antenna can generate multiple radiation nulls using multiple resonators. However, introducing multiple cross-coupling paths increases the overall size and complexity of the antenna. In Scheme 3, various filtering structures are integrated onto the antenna, encompassing etched slots on radiation patches [6,7], short-circuit pins [8], and parasitic patches [9]. In reference[9], by etching four slots on the square radiating patch, radiation nulls can be achieved in the stopband between the two operating frequency bands. The other two radiation nulls are produced by the microstrip open-circuit stepped-impedance resonator. However, the

[1]School of Optoelectronic Engineering, Chongqing University of Posts and Telecommunications, Chongqing 400065, China. [2]Pengfei Wang, Jie Hu and Shengwei Hou contributed equally to this work. ✉email: huangwen@cqupt.edu.cn

adopted differential feeding requires connecting additional components to generate differential signals, which increases insertion loss. According to the reference[10], radiation nulls are generated through loading U-shaped slots on the antenna's matasurface and introducing parasitic patches around it. Although the method of loading filtering structure can achieve good filtering response, the entire antenna design relies heavily on the experience and intuition of the designer, so it is inevitable that there would be a trial-and-error process, which needs a lot of time and a long design period.

In 2023, Chen proposed an aided design method of a filtering antenna using CMA [11]. The method analyzes the existence of modal nulls and nonmodal nulls in a filtering antenna, and greatly simplifies the design process of a filtering antenna. Nevertheless, there is no analysis about the modal weighting coefficients after feeding. As a result, it is not possible to accurately determine whether the mode is energized after feeding and consistent with previous analyses.

In the paper, a wideband filtering antenna loading with U-shaped parasitic patches based on CMA is presented. By introducing sawteeth structures on the edges of the patches, the resonant frequencies of desired modes can be adjusted, thereby enhancing the antenna's bandwidth. Furthermore, UPP are loaded to realize the bandpass filtering performance. Moreover, CMA is utilized in the antenna design process to achieve filtering capabilities.

Antenna configuration

Figure 1 illustrates the designed antenna structure with a size of 50 mm×50 mm×2.5 mm. The antenna employs two dielectric substrates of F4B material with $\varepsilon_r = 2.65$ and $\tan\delta = 0.0015$. The antenna is comprised of a central eight-sawteeth patch, four surrounding single sawtooth patches, four rectangle patches, two x-direction aligned UPP, two y-direction aligned UPP, and an L-shaped probe structure. The L-shaped probe structure is composed of a feeding probe and a patch located on the lower substrate, which is named Patch A for the convenience of subsequent description. Detailed antenna parameter values are provided in Table 1.

Filtering antenna analysis
Radiation nulls analysis

In 2023, Chen utilized CMA to categorize radiation nulls into two distinct types for the first time, introducing the concept of modal null and nonmodal null [9]. A method for predicting frequencies of nonmodal nulls by near-field change rate in resonant modes is proposed. The change rate of the total near-field electric field is given by

$$E_{\text{roc\_total}} = \frac{E_{\text{total}}(f_{i-1}) - E_{\text{total}}(f_i)}{\max\left(E_{\text{total}}(f_{i-1}), E_{\text{total}}(f_i)\right)} \tag{1}$$

where $E_{total}(f_{i-1})$ represents the total near-field electric field magnitude at the preceding frequency point f_{i-1}, whereas $E_{total}(f_i)$ denotes that at the subsequent frequency point f_i. The maximum value between the two
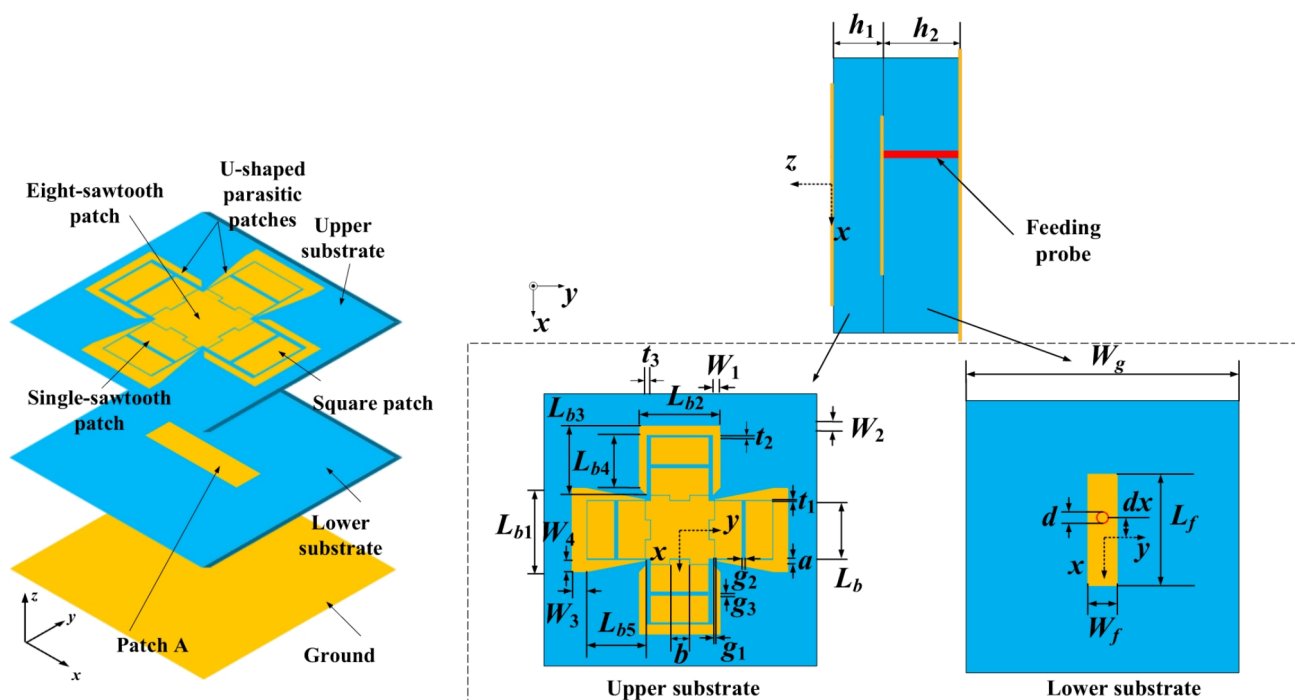

Fig. 1. The proposed antenna structure with two layers.

Parameter	size	Parameter	size	Parameter	size	Parameter	size
W_g	50	t_1	0.2	a	1.0	L_{b3}	10.6
W_1	1.1	t_2	0.5	b	2.9	L_{b4}	8.4
W_2	1.1	t_3	0.9	L_b	9.0	L_{b5}	9.2
W_3	2.0	g_1	0.15	L_{b1}	13.0	L_f	15.35
W_4	1.8	g_2	0.66	L_{b2}	13.0	W_f	2.7
d	0.94	g_3	0.62	h_1	1.5	h_2	2.0
dx	2.9						

Table 1. Detailed dimensions of the antenna. (Unit: mm)
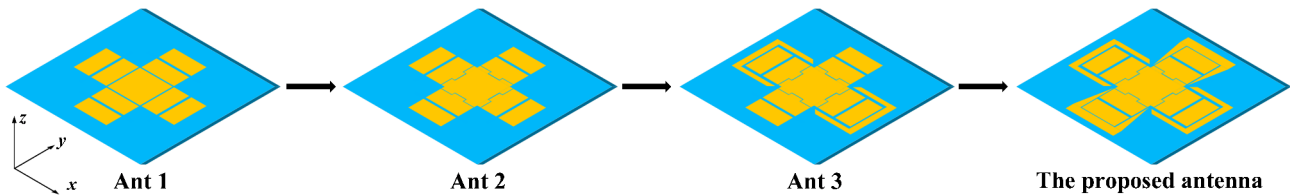
Fig. 2. The progression of the proposed filtering antenna.

adjacent total near-field electric field magnitude is expressed as max($E_{total}(f_{i-1})$, $E_{total}(f_i)$). The frequency at which a radiation null occurs signifies a pronounced inflection point in the total near-field electric field, indicative of a substantial variation in the electric field. Therefore, from the sudden change of this curve, the frequency position of the inherent nonmodal null in the resonant mode can be obtained.

Design analysis

Figure 2 shows the progression of the proposed antenna, and for the structure of Ant 1, the surface patches are without sawteeth and without UPP. While for Ant 2, sawteeth have been added on the edges of patches based on Ant 1. Based on the structure of Ant 2, Ant 3 is added a pair of UPP. And then, the finally proposed antenna is obtained by adding another pair of UPP on Ant 3. Next, the mechanism of the proposed antenna to achieve broadband and filtering functions could be analyzed through the evolution.

Ant 1 is only composed of nine rectangular patches. In this design, the goal is designing an x-direction linearly polarized antenna, thus all the x-direction linearly polarized modes of Ant 1 need to be found out. MS curves is observed in Fig. 3, and modal currents and modal fields of Ant 1 are depicted in Fig. 4. It is found that only J_1 and J_8 are linearly polarized modes in the x-direction on the all patches on the upper substrate, while the modal current on Patch A of the L-shaped probe is also linearly polarized in the x-direction. And the current magnitudes of all patches including Patch A are not weak, so the two modes are linearly polarized modes that can be excited. The modal currents of other modes such as J_2 and J_3 on the upper substrate patches is not in the desired x-direction, and the current on Patch A of the L-shaped is not in the x-direction, but fortunately the current magnitudes are weak, so the modes cannot be excited to affect the performance of the antenna. When J_1 and J_8 are simultaneously excited, due to the relatively large frequency spacing about 2.56 GHz between their resonant frequencies, the bandwidth formed by J_1 and J_8 is difficult to form a broadband.

To achieve a broadband performance, it is necessary to simultaneously excite J_1 and J_8 of Ant 1, whereas with their resonant frequencies separated by a relatively small frequency spacing. Therefore, Ant 2 is obtained by modifying the center patch into an eight-sawtooth patch, and modifying the surrounding patches into single-sawtooth patches. The added sawteeth effectively lengthens the patch current paths by employing the meandering technique, which leads to a larger effective length of patches on the upper substrate resulting in a decrease of the antenna's resonant frequency. As shown in Fig. 5, the resonance interval between the excitable modes J_1 and J_8 required by Ant 2 is reduced from 2.56 GHz of Ant 1 to 1.93 GHz.

However, as shown in Fig. 6, where the modal currents on the upper substrate patches of other modes including J_2, J_3, and J_5, are not only in the x-direction, and the currents on Patch A of these modes do not only have one direction with x-direction, which makes them difficult to be excited. So, these modes could not have a negative effect on the antenna's performance. The frequency band between 3 GHz and 8 GHz lacks additional excitable modes, allowing Ant 2 to potentially exhibit radiation nulls. The absence of modal nulls in this frequency band indicates that nonmodal nulls may be hidden in J_1 and J_8.

Figure 7 displays both the total near-field electric field intensity curve pertaining to J_8 and its accompanying variation rate *roc_E_total*. From Fig. 7(a), the total near-field electric field amplitude of J_1 shows no significant inflection point between 3 GHz and 5 GHz, indicating that there are no nonmodal nulls embedded in J_1. In Fig. 7(b), a distinct inflection point is found in the total near-field electric field amplitude of J_8 at 7 GHz. As shown in Fig. 7(c), it is easy to identify the exact frequency point of the nonmodal null, which corresponds to the frequency with a zero-change rate. As highlighted by the red circle depicted in Fig. 8(c), the nonmodal null is located at 7.05 GHz.
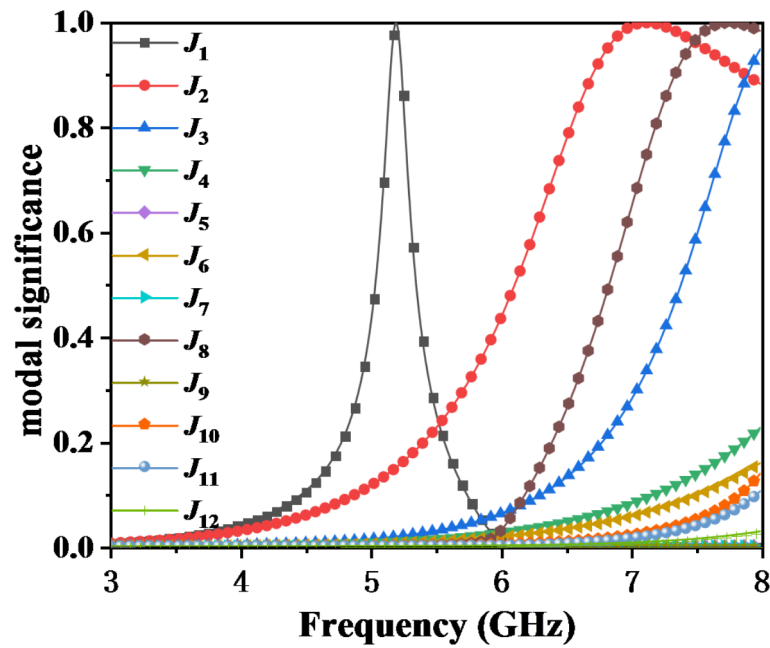
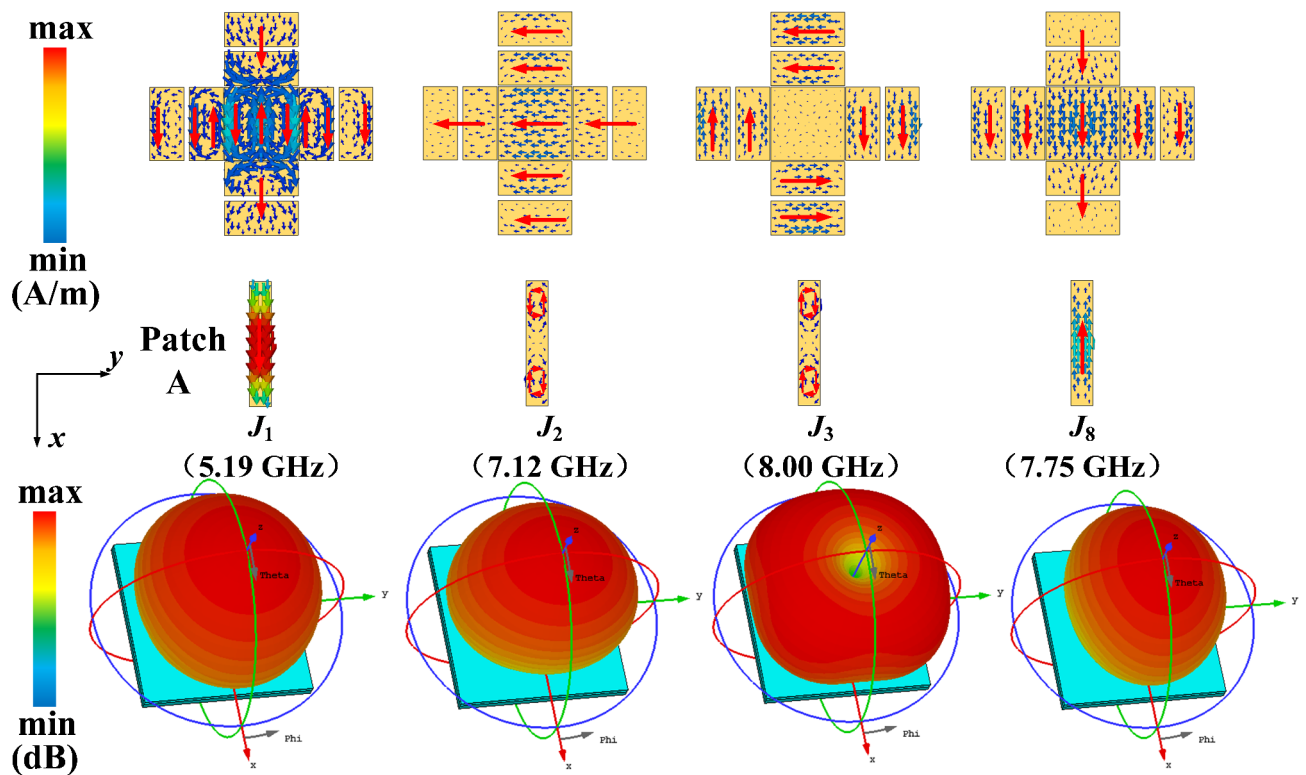**Fig. 3**. Modal significance curves of Ant 1.

Fig. 4. Modal currents and radiation patterns of Ant 1.

The resonant mode arises at the location of maximum electric field intensity on Patch A, whereas the nonmodal null emerges precisely where the electric field attains its minimum value. However, J_8 is at 6.99 GHz, while the nonmodal null is at 7.05 GHz. The electric field magnitude along the x-axis is shown in Fig. 1.on Patch A is presented in Fig. 8, with frequencies of 6.99 GHz for J_8 and 7.05 GHz for J_8'null. It is inherently infeasible to concurrently attain the strongest and weakest electric field intensities at the same position within a
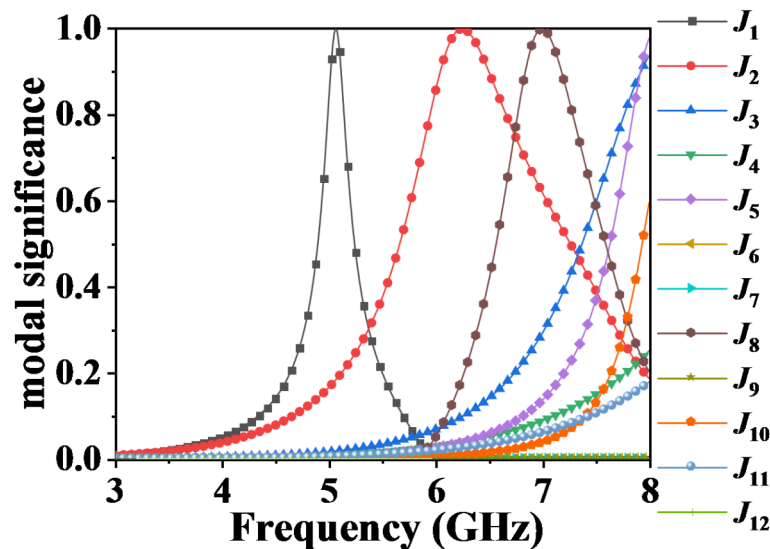
Fig. 5. Modal significance curves of Ant 2.
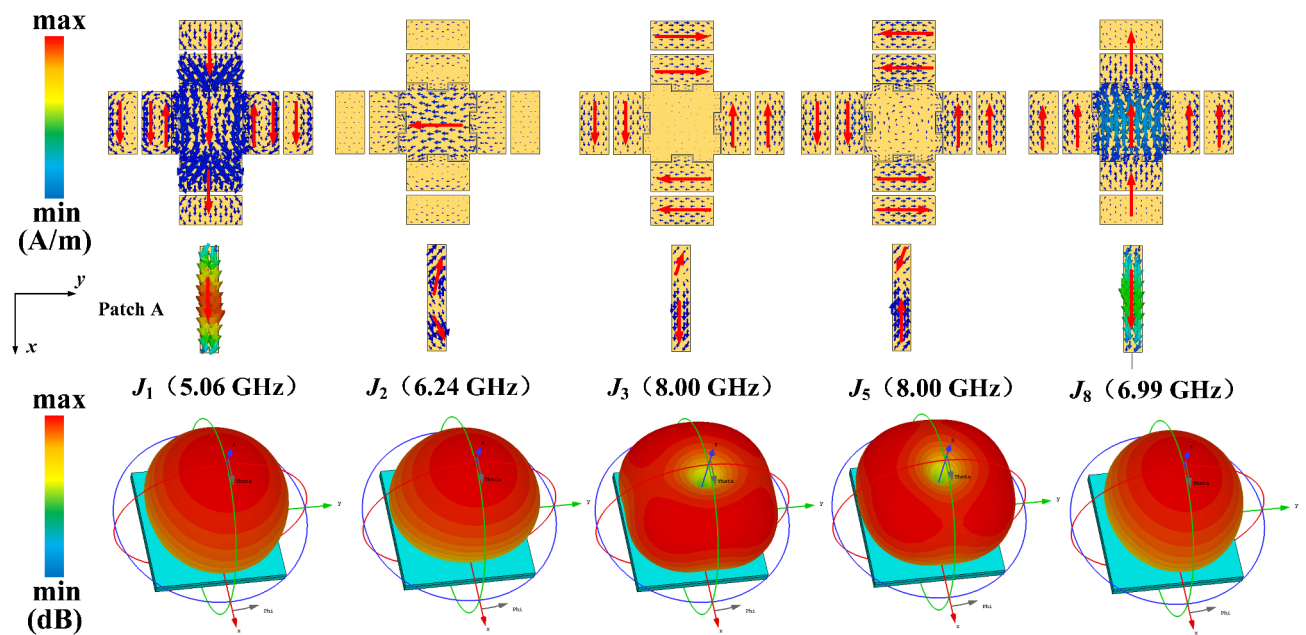
Fig. 6. Modal currents and radiation patterns of Ant 2.

narrow frequency range, thereby impeding the fulfillment of excitation position criteria and the establishment of effective out-of-band suppression.

The incorporation of a UPP pair to constitute Ant 3 aims at augmenting Ant 2's capability to suppress high-frequency out-of-band signals. The inclusion of UPP is aimed at achieving radiation nulls. At the frequencies corresponding to radiation nulls, the surface current becomes concentrated on the UPP. Consequently, power is not radiated effectively, leading to excellent filtering performance. Simultaneously, the UPP generates currents of opposite phase to those on the radiating patch, resulting in zero radiation. For a more concise analysis, Fig. 9(a) only shows Ant 3's excitable modes. A new excitable mode, named as J_9, has emerged within the frequency band. After loading the UPP, the rectangular patches and single sawtooth patches on both sides in the y-direction generate reverse x-direction currents when observing the modal current of J_9 in Fig. 9 (b). These reverse currents can offset part of the positive x-direction currents on the remaining patches. At the same time, the modal field of J_9 has two lobes in the $+x$ direction and $-x$ direction respectively. However, whether the surface currents on all patches of J_9 can offset completely to form a radiation null remains uncertain and needs to be analyzed.

To obtain the nonmodal null frequencies of J_7 and J_9, the near-field electric field magnitudes of J_7 and J_9 and the variation rate E_{roc_total} are calculated out with formulas (1) and plotted in Fig. 10. Evidently, the total
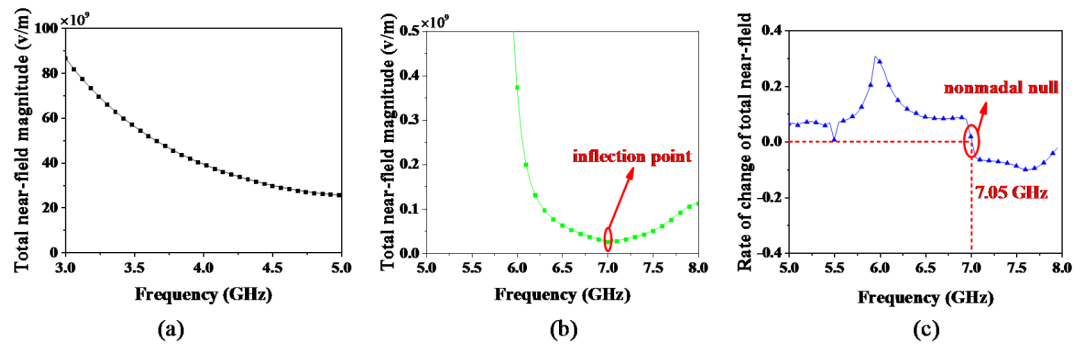
Fig. 7. Nonmodal null judgement curve (**a**) Total near-field electric field magnitudes of J_1. (**b**) Total near-field electric field magnitudes of J_8. (**c**) The variation rate E_{roc_total} of J_8.
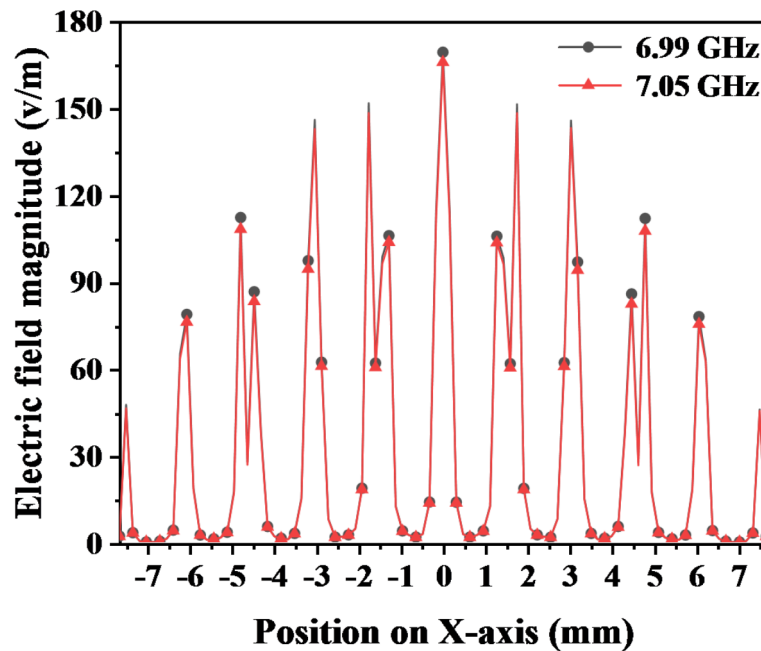

Fig. 8. The electric field magnitude along *x*-axis on Patch A at 6.99 GHz for J_8 and 7.05 GHz for J_8'null.

near-field electric field amplitude of both J_7 and J_9 undergoes notable inflections within the high-frequency band, specifically at approximately 7.6 GHz for J_7 and 7.5 GHz for J_9, respectively, hinting at the presence of nonmodal nulls at these frequencies. From Fig. 9 (b), the precise frequency of the inflection point in the total near-field electric field, where the rate of change is null, can be discerned with clarity. As shown by the red circle in the Fig. 10 (b), the nonmodal null point of J_7 is at 7.67 GHz and that of J_9 is at 7.48 GHz. Therefore, the high-frequency nonmodal null are successfully achieved outside the bandwidth and can enhance out-of-band suppression. But until now, there is no radiation null in the low-frequency range.

To achieve a low-frequency radiation null for Ant 3 to improve low-frequency stopband suppression, another pair of UPP are added to Ant 3, resulting in the final proposed antenna structure. As observed in Fig. 11, among MS curves, J_8,J_9, and J_{11} of the final proposed antenna is corresponded to J_2,J_7, and J_9 of Ant 3. A newly produced J_2 is appeared to the lower frequency band of the desired linearly polarized J_8, and the curve of J_2 changes rapidly, in keeping with the characteristics of a modal null. As show in Fig. 11(b), the modal current of J_2 indicates that at 4 GHz the currents on all patches are opposite to each other. Meanwhile, the MS curve of J_2 changes rapidly, proving that a modal null point is generated at 4 GHz.

After analyzing the characteristic modes of the antenna patches, the resonant frequencies and radiation null frequencies have been identified. The optimal exciting position is selected by the electric field amplitude, where the electric field should be weakest at non-modal nulls and strongest at modal nulls. For target resonant modes (J_2, J_8, and J_9), the location of the strongest electric field intensity needs to be found out, whereas for non-target modes (J_{11}), the location of the weakest electric field intensity should be sought. Specifically, the point of feeding for J_9'null and J_{11}'null ought to be selected at the location where the intensity of the electric field is minimal.
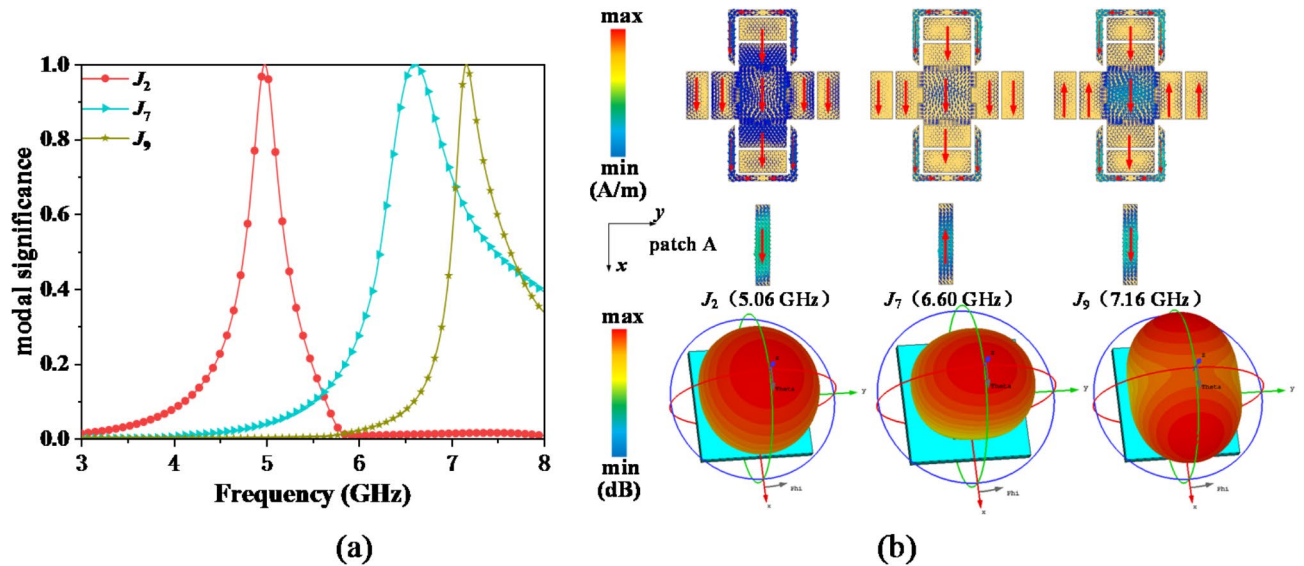
Fig. 9. CMA of Ant 3. (**a**) MS curves for Ant 3. (**b**) Modal currents and radiation patterns of Ant 3.
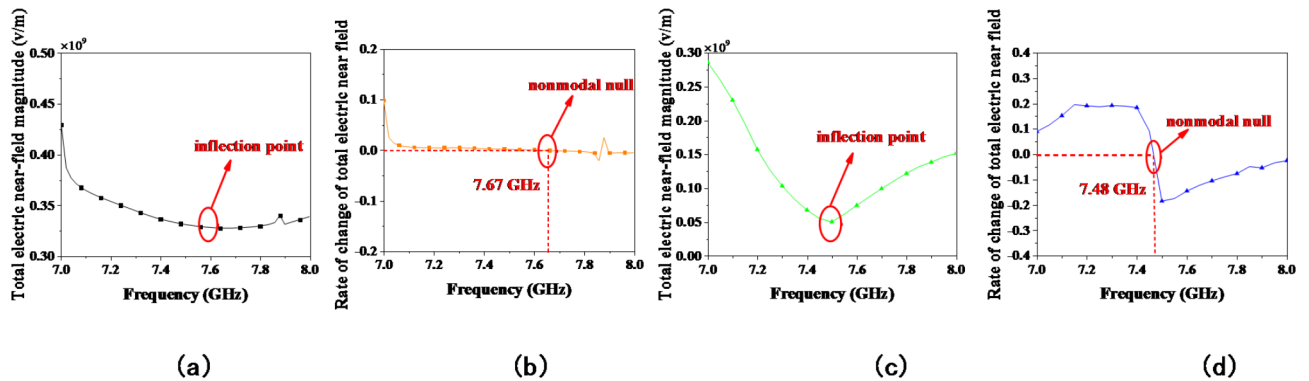

Fig. 10. Nonmodal null judgement curve. (**a**) Total near-field electric field magnitudes of J_7. (**b**) The variation rate E_{roc_total} of J_7. (**c**) Total near-field electric field magnitudes of J_9. (**d**) The variation rate E_{roc_total} of J_9.

Figure 12 depicts the electric field amplitude distribution along x-axis as marked in Fig. 1. It showcases the profiles at the resonant frequencies of four distinct modes, as well as the frequencies corresponding to two radiation nulls. The optimal feeding locations for J_2, J_8, J_9, and their respective nulls J_9'null, J_{11}'null, along with J_{11}, are specified as $x = 0$ mm for the former three, $x = \pm 6.77$ mm for J_9'null and J_{11}'null, and $x = \pm 6.9$ mm for J_{11}. To meet the feeding requirements as much as possible, the optimal feeding position is compromised and determined at $x = \pm 3.03$ mm. With subsequent feeding optimization, the feeding position is set to $x = 2.9$ mm.

Lastly, the simulated S-parameters and gains of the antennas during the evolution are depicted in Fig. 13. It is found that the proposed antenna is produced radiation nulls at 4 GHz and at 7.45 GHz. This is consistent with the CMA. After excitation, MWC is shown in Fig. 14(a), it is observed that both linearly polarized modes of J_8 and J_9 can be effectively excited. Figure 14(b) shows the simulated results, revealing an impedance bandwidth spanning 26.86% from 4.93 GHz to 6.46 GHz.

Parametric analysis

In this section, a parametric study is conducted to elucidate more clearly the influence of key parameters on radiation nulls. The study also analyzes various feeding positions and unveils the intrinsic relationship between radiation nulls and out-of-band selectivity. Previously, the operating principle of the antenna has been explored, highlighting the correlation between radiation nulls and UPP. Specifically, as shown in Fig. 15(a), the stopband suppression level of high-frequency radiation nulls is closely tied to parameter W_2. As W_2 increases, the radiation suppression level of high-frequency stopband is enhanced, owing to a more concentrated distribution of surface currents on the UPP, which subsequently reduces the effective radiated power. Furthermore, as shown in Fig. 15(b), the specific frequency of high-frequency nulls is associated with parameter W_3. As W_3 increases, the high-frequency radiation nulls are shifted towards lower frequencies. This is primarily due to the UPP generating currents opposite in phase to the radiation patch, which intensify with increasing W_3, thereby causing
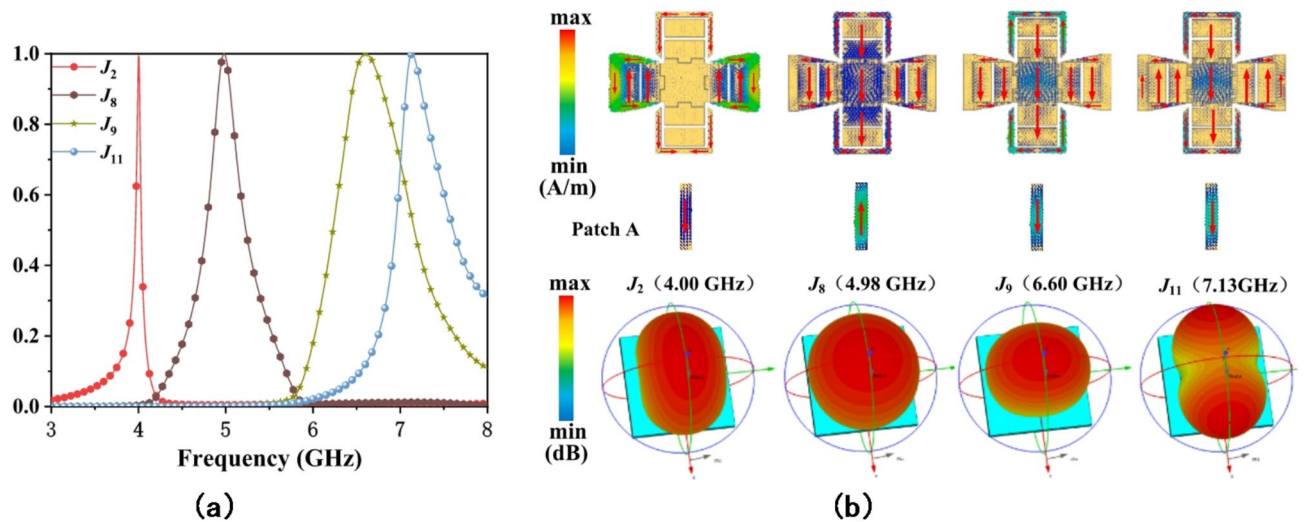
Fig. 11. CMA of the proposed. (**a**) MS curves for the proposed antenna. (**b**) Modal currents and fields of the proposed antenna.
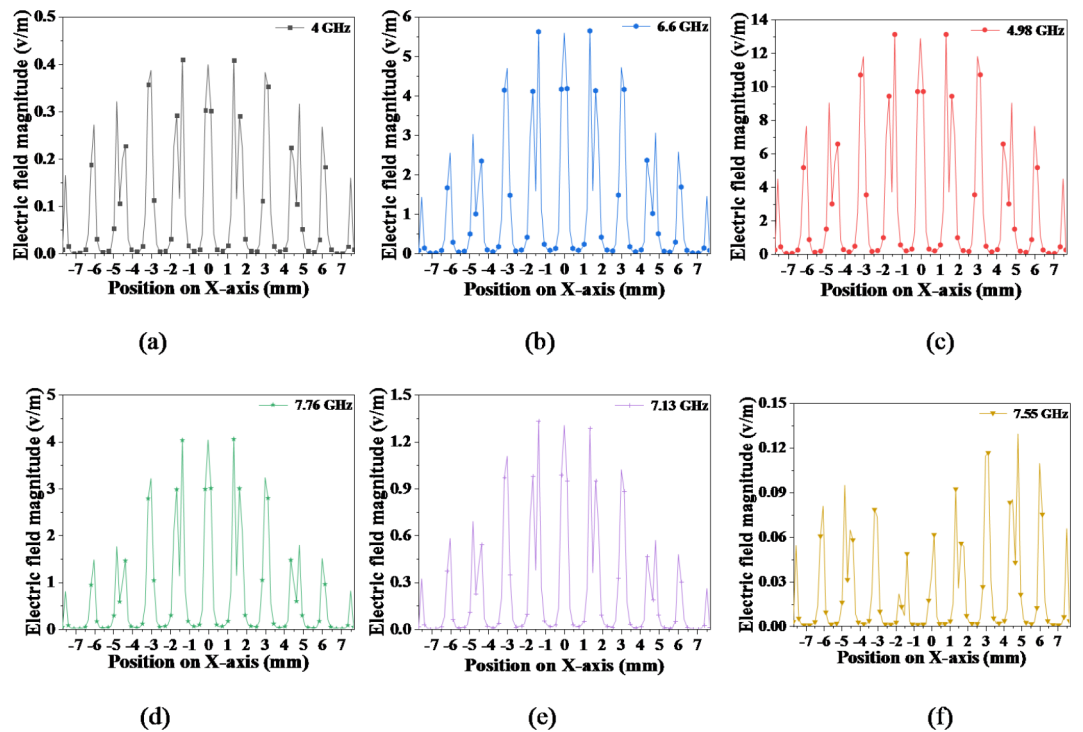

Fig. 12. The electric field magnitude along the $y=0$ on Patch A (**a**) at 4 GHz for J_2. (**b**) at 4.98 GHz for J_8. (**c**) at 6.6 GHz for J_9. (**d**) at 7.67 GHz for J_9'null. (**e**) at 7.13 GHz for J_{11}. (**f**) at 7.55 GHz for J_{11}'null.

the radiation nulls to shift towards lower frequencies. As shown in Fig. 15(c), for low-frequency radiation nulls, their position is influenced by parameter Lb_5. An increase in Lb_5 results in a larger chamfer on the UPP arm, which reduces the concentration of surface currents on the UPP and shifts the radiation nulls towards lower frequencies. As shown in Fig. 15(d), in terms of feeding positions, as the feeding position dx increases, the S-parameters of the antenna align more closely with the desired mode matching effect in characteristic mode analysis. In summary, by finely tuning these key parameters, the optimal design of broadband filtering antennas can be achieved.
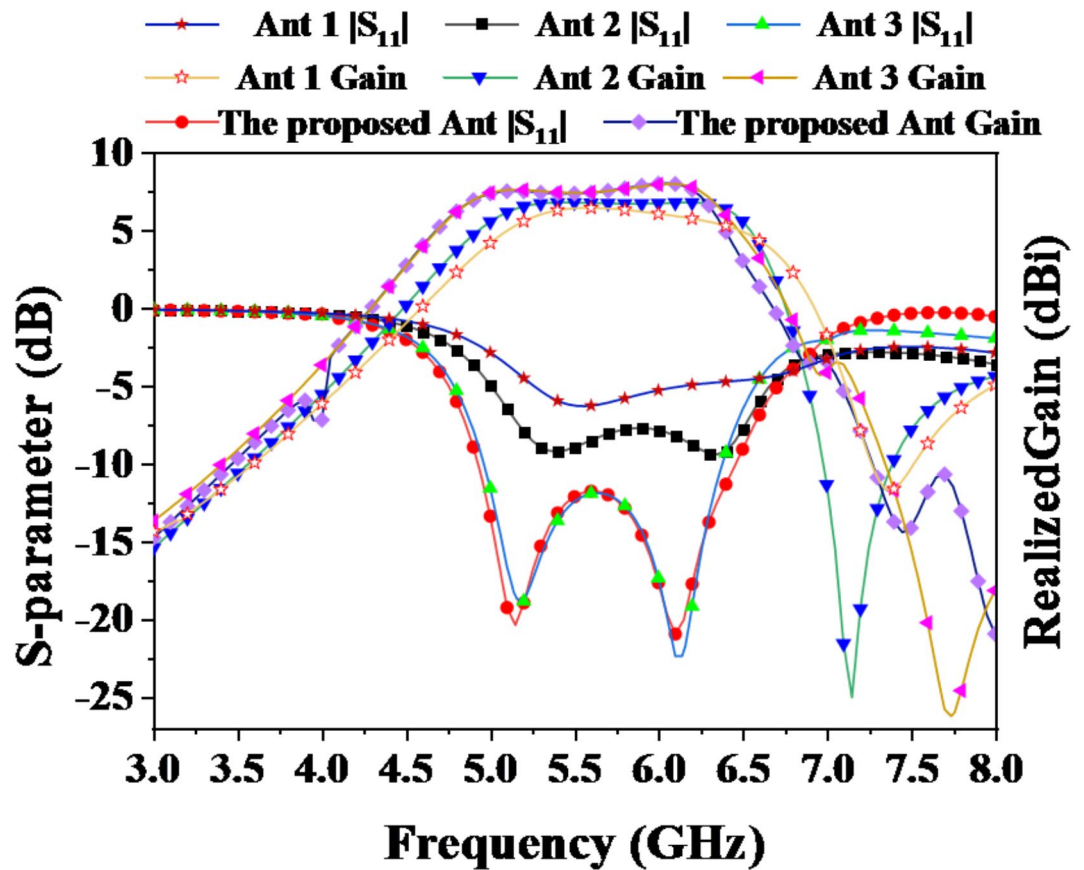
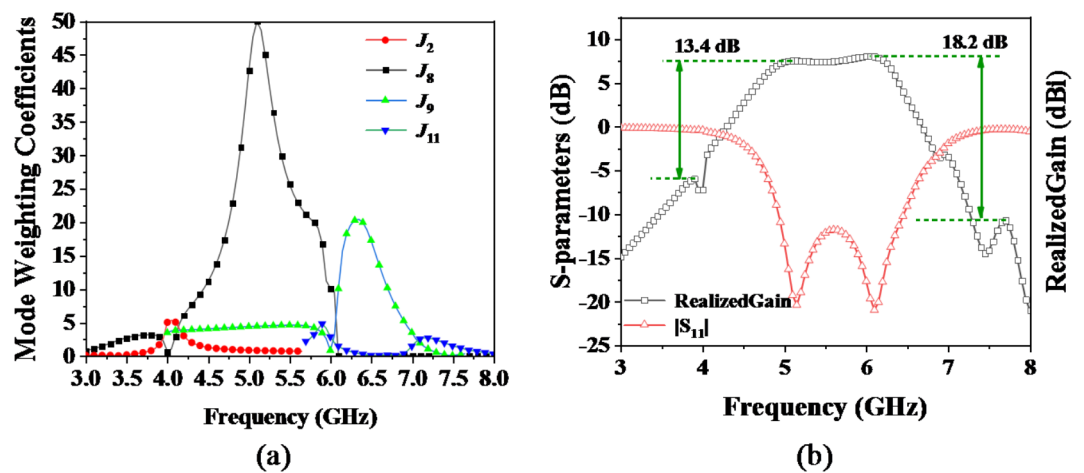**Fig. 13**. S-parameters and realized Gains for the evolution of the proposed antenna.

Fig. 14. The simulations of the proposed antenna. (**a**) MWC. (**b**) S-parameters and gain.

Measurement analysis

To evaluate the performance of the designed filtering antenna, a prototype has been fabricated, as depicted in Fig. 16. Subsequently, the experimental outcomes, including the measured S-parameters and gain profiles, are illustrated in Fig. 17. The measured operational frequency range is from 5 GHz to 6.52 GHz of $|S_{11}|$ less than −10 dB, resulting in a relative bandwidth of 26.38%. Within this passband, there are two resonant frequency points at 5.15 GHz and 6.35 GHz. At 4 GHz, a radiation null is discerned, exhibiting a suppression level of 12.3 dB. Conversely, at 7.45 GHz, a radiation null is detected, featuring a higher suppression level of 17.8 dB. As shown in Fig. 18, the radiation efficiency of the antenna within its operating frequency band is greater than 92%. Furthermore, Fig. 19 illustrates the radiation patterns exhibited by the proposed filtering antenna when
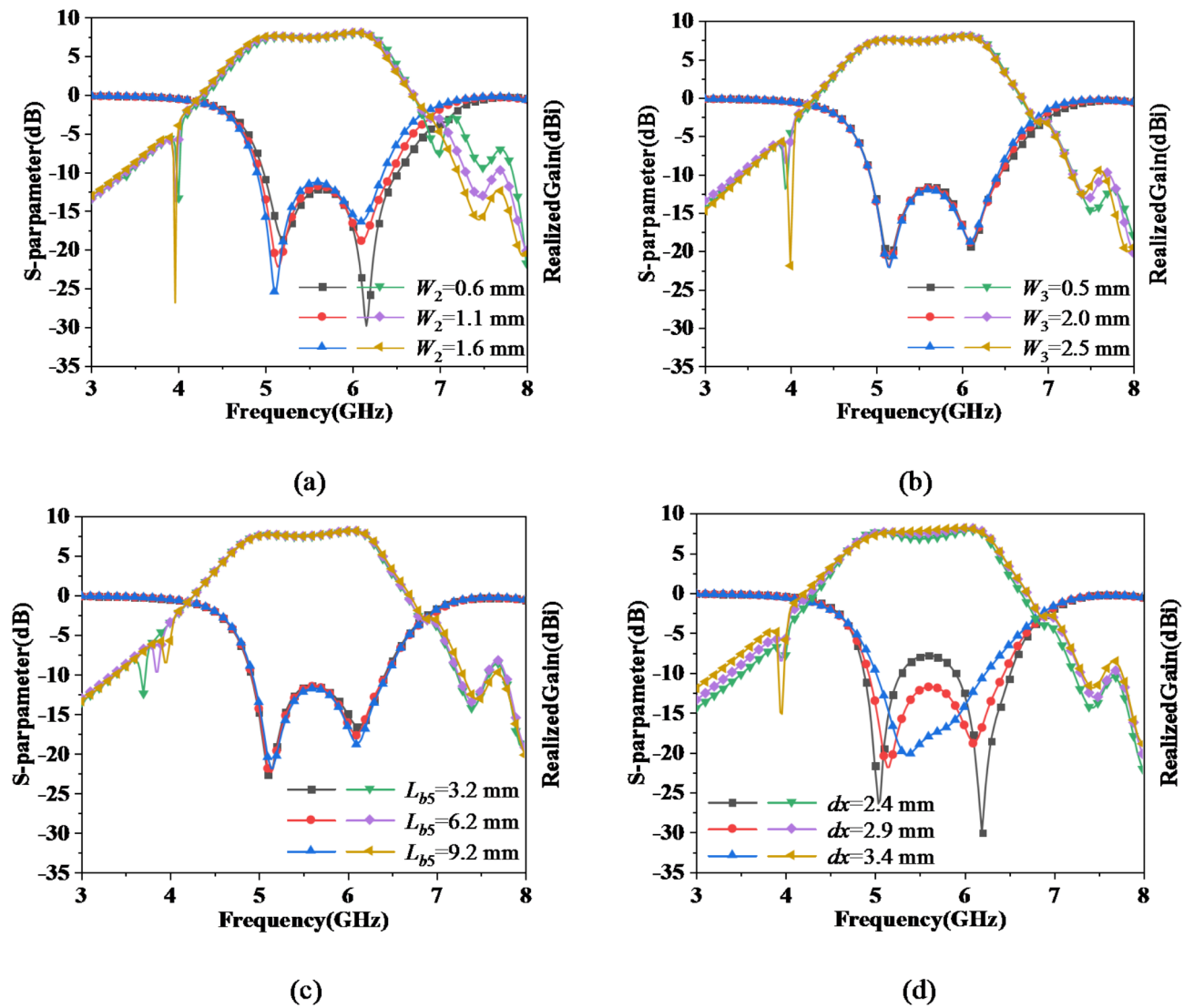
Fig. 15. The simulations of key parameters. (**a**) W_2. (**b**) W_3. (**c**) L_{b5}. (**b**) dx.
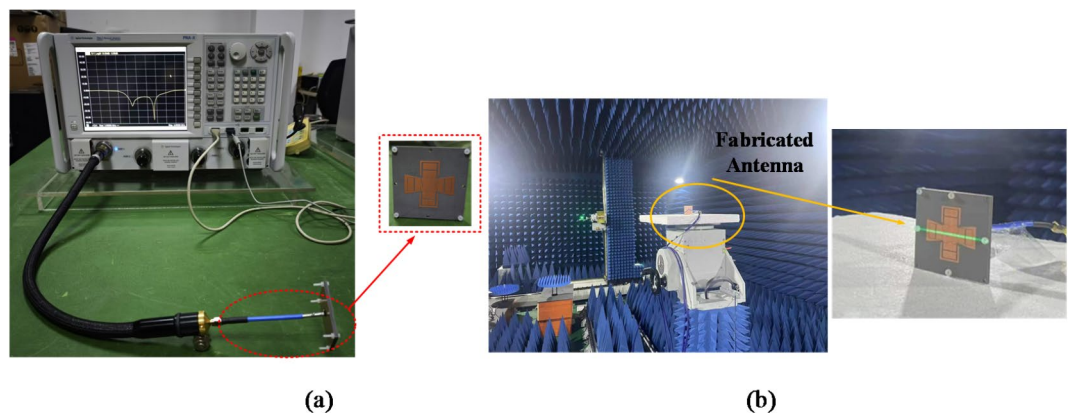

Fig. 16. The fabricated antenna and measuring environment. (**a**) The vector network analyzer for measuring S-parameters. (**b**) The anechoic chamber for measuring the radiation patterns.
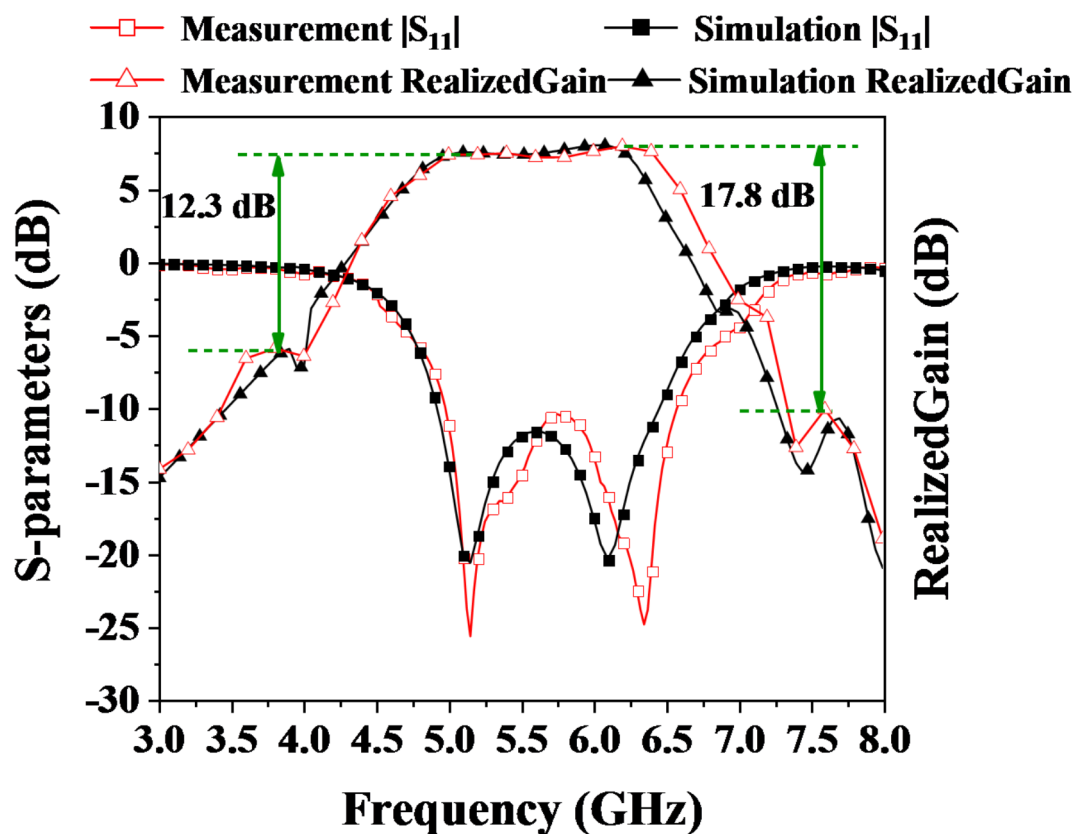
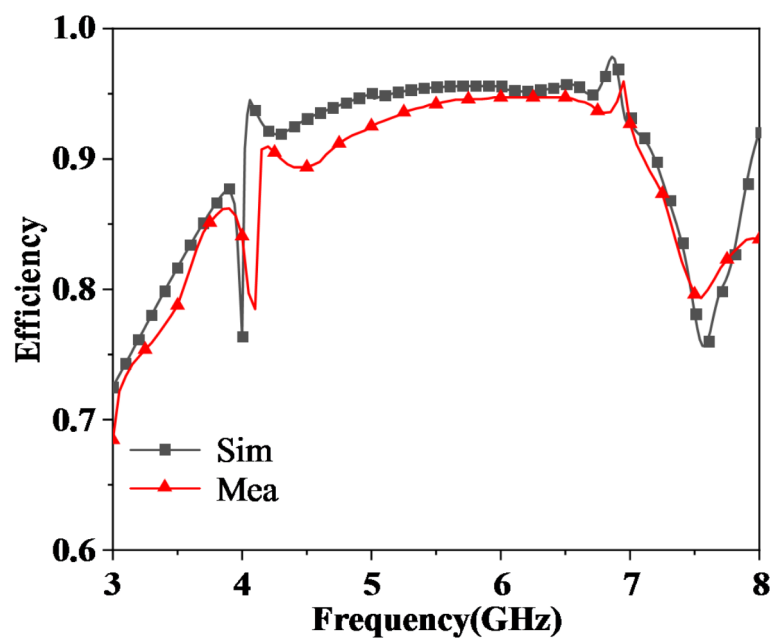**Fig. 17**. Simulated and measured S-parameters and gain.

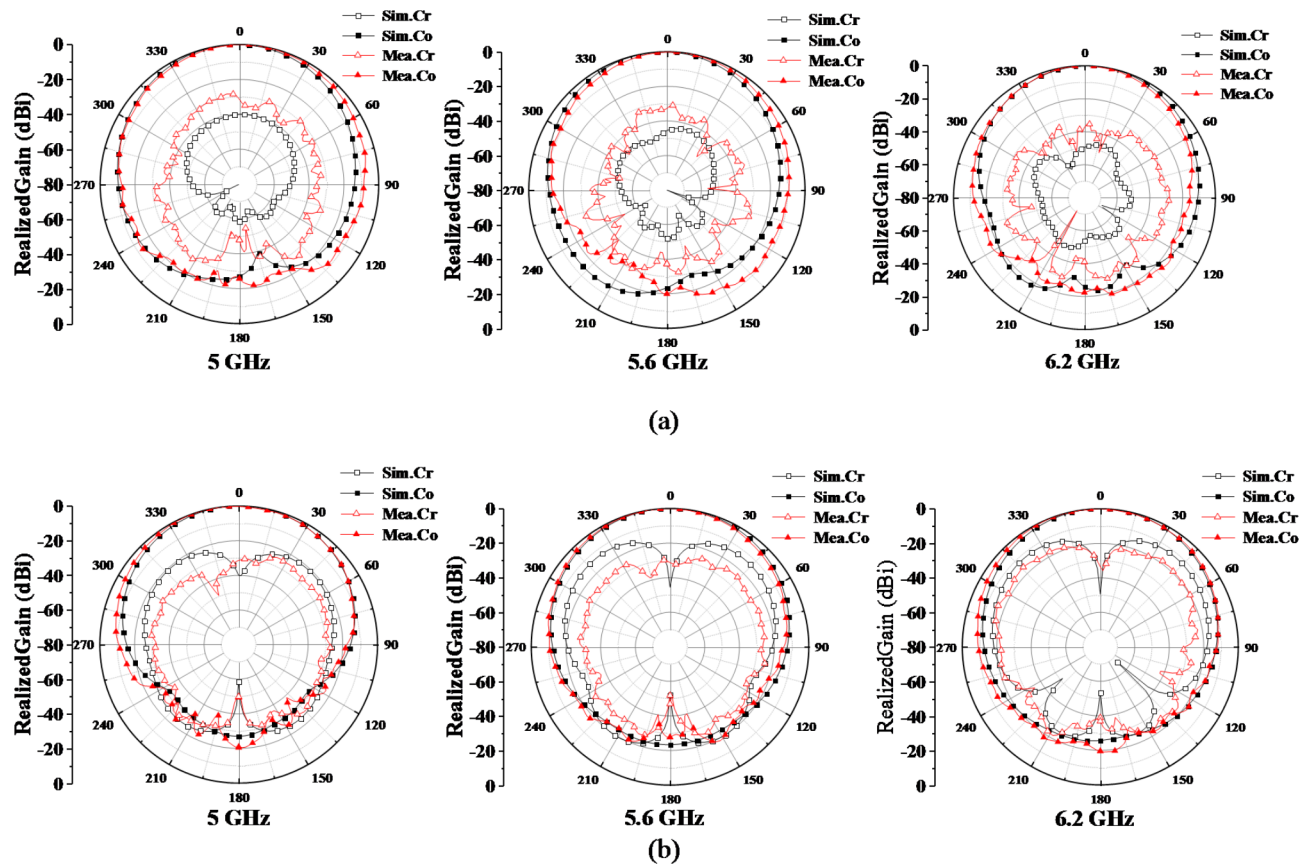**Fig. 18**. Simulated and measured antenna efficiency.

Fig. 19. Radiation patterns (**a**) *xoz* plane. (**b**) *yoz* plane.

Ref.	Size(λ_0^3)	-10 dB Bandwidth	Max Gain (dBi)	Cross-polarization (dB)	Suppression ratio @low/high (dB)	Efficiency	Layers
10	$0.77 \times 0.77 \times 0.09$	17.6%	8	<-20	17.4	-	2
12	$1.3 \times 1.3 \times 0.06$	28.4%	8.2	<-25	>20	-	2
13	$1.2 \times 1.2 \times 0.032$	20.1%	9.5	<-20	14.5/16	>88%	1
14	$1.15 \times 1.15 \times 0.09$	19.6%	9.7	<-22	>21.5	-	2
15	$0.58 \times 0.58 \times 0.05$	16.1%	9.6	<-20	>15	>98%	2
16	$1.3 \times 1.0 \times 0.05$	14.4%	11.1	-	17.8/17.9	>75%	5
17	$0.69 \times 0.47 \times 0.02$	5.1%	6.3	-	>14	-	1
18	$0.6 \times 0.47 \times 0.02$	9.2%	5.8	<-20	>11	-	1
Proposed	$0.94 \times 0.94 \times 0.066$	26.38%	7.98	<-31	12.3/17.8	>92%	2

Table 2. Comparison with recently reported filter antennas.

subjected to port excitation. In the operational frequency range, the cross-polarization level remains under −31 dB. The discrepancies between the measurements and simulation results stem primarily from manufacturing inaccuracies and inherent measurement errors. During the assembly process of the proposed multilayer antenna, each layer is fabricated separately and joined together using plastic screws. This process often leads to imprecise alignment between the layers, which in turn affects the antenna's performance.

In Table 2, a comparative performance analysis of the proposed linearly polarized filtering antenna with other recent filtering antenna designs is represented. The bandwidth listed in Table 2 is corresponded to the frequency range where both the $|S_{11}|$ is less than −10 dB and the gain variation remains within 3 dB. The proposed design offers several advantages, including a wide bandwidth, bandpass filtering capabilities, a low profile, compact dimensions, and low cross-polarization level.

Conclusion

In this paper, a filtering antenna loaded with UPP using CMA is proposed. An L-shaped probe structure is employed to feed the antenna. Within the operating frequency band, two line-polarized radiation modes are

excited efficiently, thus achieving a broadband effect. To achieve a broader bandwidth, the sawteeth structures enable the two distinct characteristic modes to be closer with a smaller frequency space while allowing them to coexist within the operating frequency band. Additionally, utilizing UPP effectively creates radiation nulls in both the lower and upper frequency bands, which lie outside of the passband, thereby enhancing its out-of-band rejection capabilities significantly. Consequently, the proposed antenna boasts advantages such as broadband, bandpass filtering, low profile, compact size, and low cross-polarization. Therefore, it holds potential for application in 5G base stations, terminal devices, and other scenarios, thereby enhancing communication quality and stability.

Data availability

The datasets generated during the study are available from the corresponding author on reasonable request.

References

1. Guo, J., Chen, Y. & Yang, D. Design of a Circuit-Free filtering metasurface antenna using characteristic mode analysis. *IEEE Trans. Antennas Propag.* **70**(12), 12322–12327 (2022).
2. Feng, F., Liu, X. X. & Zhao, X. B. A differential low-profile metasurface filtering antenna. In *Proceedings of the IEEE Symposium on Antennas and Propagation (ISAP)*, 61–62 (2022).
3. Zhao, C. X., Pan, Y. M. & Su, G. D. Design of filtering dielectric resonator antenna arrays using simple feeding networks. *IEEE Trans. Antennas Propag.* **70**(8), 7252–7257 (2022).
4. Chuang, C. T. & Chung, S. J. Synthesis and design of a new printed filtering antenna. *IEEE Trans. Antennas Propag.* **59**(3), 1036–1042 (2011).
5. Zhang, B. & Xue, Q. Filtering antenna with high selectivity using multiple coupling paths from source/load to resonators. *IEEE Trans. Antennas Propag.* **66**(8), 4320–4325 (2018).
6. Li, J. F., Wu, D. L., Gary, Z. & Wu, Y. J. Mao. A left/righthanded dual circularly-polarized antenna with duplexing and filtering performance. *IEEE Access.* **7**, 35431–35437 (2019).
7. Li, J. F., Chen, Z. N. & Wu, D. L. Dual-beam filtering patch antennas for wireless communication application. *IEEE Trans. Antennas Propag.* **66**(7), 3730–3734 (2018).
8. Li, Y., Zhao, Z., Tang, Z. & .Yin, Y. Differentially fed, dual-band dualpolarized filtering antenna with high selectivity for 5G sub-6 ghz base station applications. *IEEE Trans. Antennas Propag.* **68**(4), 3231–3236 (2020).
9. Qian, J. F., Chen, F. C. & Chu, Q. X. A novel electric and magnetic gap-coupled broadband patch antenna with improved selectivity and its application in MIMO system. *IEEE Trans. Antennas Propag.* **66**(10), 5625–5629 (2018).
10. Yang, W. et al. Novel filtering method based on metasurface antenna and its application for wideband high-gain filtering antenna with low profile. *IEEE Trans. Antennas Propag.* **67**(3), 1535–1544 (2018).
11. Chen, X. J., Lai, Q. X. & Pan, Y. M. Characteristic-Mode-Analysis-Aided design of filtering patch antennas. *IEEE Trans. Antennas Propag.* **71**(3), 2224–2234 (2023).
12. Pan, Y. M. et al. A low-profile high-gain and wideband filtering antenna with metasurface. *IEEE Trans. Antennas Propag.* **64**(5), 2010–2016 (2016).
13. Yang, D., Zhai, H. & Guo, C. A compact single-layer wideband microstrip antenna with filtering performance. *IEEE Antennas. Wirel. Propag. Lett.* **19**(5), 801–805 (2020).
14. Zhang, X. Y., Duan, W. & Pan, Y. M. High-gain filtering patch antenna without extra circuit. *IEEE Trans. Antennas Propag.* **63**(12), 5883–5888 (2015).
15. Li, L., Xiong, H. D. & Wu, W. Y. A T-Shaped strips loaded wideband filtering patch antenna with high selectivity. *IEEE Antennas. Wirel. Propag. Lett.* **1**(23), 89–93 (2023).
16. Wang, T., Yan, N., Tian, M., Luo, Y. & Ma, K. A low-cost high-gain filtering patch antenna with enhanced frequency selectivity based on SISL for 5G application. *IEEE Antennas. Wirel. Propag. Lett.* **21**(9), 1772–1776 (2022).
17. Hu, K. Z., Tang, M. C., Li, D., Wang, Y. & Li, M. Design of compact, single-layered substrate integrated waveguide filtering antenna with parasitic patch. *IEEE Trans. Antennas Propag.* **68**(2), 1134–1139 (2020).
18. Hu, K. Z. et al. Low-profile single-layer half-mode SIW filtering antenna with shorted parasitic patch and defected ground structure. *IEEE Trans. Circuits Syst. II Express Briefs.* **70**(1), 91–95 (2022).

Acknowledgements

Author contributions

Wen Huang supervised the research work and Pengfei Wang helped in funding the research work and Jie Hu reviewed the results and Shengwei Hou followed the experimental works and wrote the main manuscript text. All authors reviewed the manuscript.

Declarations

Competing interests

The authors declare no competing interests.

Additional information

Correspondence and requests for materials should be addressed to W.H.

Reprints and permissions information is available at www.nature.com/reprints.

Publisher's note Springer Nature remains neutral with regard to jurisdictional claims in published maps and institutional affiliations.